Numerical Heat Transfer, Part A: Applications: An International Journal of Computation and Methodology
Publication details, including instructions for authors and subscription information:
http://www.tandfonline.com/loi/unht20

HEAT TRANSFER ENHANCEMENT BY MULTILOBE VORTEX GENERATORS: EFFECTS OF LOBE PARAMETERS

Yeng-Yung Tsui, Shiann-Woei Leu, Chih-Chang Lin, Po-Wenn Wu
Published online: 29 Oct 2010.

To cite this article: Yeng-Yung Tsui, Shiann-Woei Leu, Chih-Chang Lin, Po-Wenn Wu (2000) HEAT TRANSFER ENHANCEMENT BY MULTILOBE VORTEX GENERATORS: EFFECTS OF LOBE PARAMETERS, Numerical Heat Transfer, Part A: Applications: An International Journal of Computation and Methodology, 37:6, 653-672

To link to this article: http://dx.doi.org/10.1080/104077800274136

Numerical Heat Transfer, Part A, 37:653–672, 2000

1040–7782/00 $12.00 + .00

HEAT TRANSFER ENHANCEMENT BY MULTILOBE VORTEX GENERATORS: EFFECTS OF LOBE PARAMETERS

Yeng-Yung Tsui, Shiann-Woei Leu, Chih-Chang Lin, and Po-Wenn Wu

Department of Mechanical Engineering, National Chiao Tung University, Hsinchu 300, Taiwan, R.O.C.

A three-dimensional computational method is developed to study the flow and heat transfer in a circular tube with a multilobe vortex generator inserted. Governing equations are discretized by the finite volume technique. The irregular lobe geometry is treated using curvilinear nonstaggered grids. Examination of the flow field reveals that the radial and counterradial flows induced inside and outside the lobe are forced to form axial vortices downstream of the vortex generator. Because of the transport of the high-speed, low-temperature core flow toward the tube wall by the vortex, heat transfer is enhanced. Also because of the vortex flow, the high-temperature wall flow is carried away from the wall to mix with the low-temperature core flow. Consequently, very effective augmentation in the heat transfer and mixing of flow temperature results. It is shown also that since the slope of the lobe is increased by enlarging the lobe penetration, reducing the lobe length, and making a concave contour geometry, the circulation, representing the strength of the axial vortex induced by the lobe, is promoted, leading to higher heat transfer and flow mixing. By increasing the lobe number both the circulation and Nusselt number (Nu) decrease because of the narrowed lobe passage.

INTRODUCTION

Energy and cost considerations have encouraged the development of more efficient heat exchange equipment. Many research works have been directed toward the development of a variety of heat transfer enhancement techniques, including modification of the heat exchange surface with ribs or fins [1–5], use of inserts such as twisted tapes or axially supported disks [6–9], and so on. By these methods, the heat exchange rate is increased via intensification of turbulence, enlargement of contact area, or increase of velocity near wall, and so on. However, the increased heat transfer is accompanied by the increase of pressure drop. Therefore, the design of an effective heat exchange system is aimed mainly at achieving a given heat transfer augmentation with minimum increase in pressure loss.

Among the objects inserted in the flow passage to improve heat transfer, the twisted tape [6–8] is one of the most extensively used. Heat transfer enhancement caused by the twisted tape occurs mainly for the following reason. The twist of the

Received 9 November 1999; accepted 7 December 1999.

This work was supported by the National Center for High-Performance Computing under Contract NCHC 86-06-010 and the National Science Council under Contract NSC 87-2212-E009-038.

Address correspondence to Professor Yeng-Yung Tsui, Department of Mechanical Engineering, National Chiao Tung University, 1001 Ta Hsueh Road, Hsinchu, Taiwan 30050, Republic of China.

NOMENCLATURE

C_f	skin friction coefficient	U^i	cylindrical velocity tensor
d	diameter of tube	u_m	mean axial velocity at inlet
E	heat transfer enhancement factor	W^i	contravariant velocity tensor
f	friction factor	x, y	Cartesian coordinates
F	friction penalty factor	z, r, ϕ	cylindrical coordinates
h, H	lobe penetration	Z, R	dimensionless coordinates
J	Jacobian of transformation	Γ	circulation
l, L	lobe length	Γ_φ	diffusivity of φ
l_t	total tube length	η	efficiency index
n	number of lobes	φ	dependent variable
Nu	Nusselt number	θ	dimensionless temperature
$\overline{\text{Nu}}$	mean Nusselt number	ρ	density
p, P	pressure	τ	shear stress
Pr	Prandtl number	ξ^i	curvilinear coordinates
P_t	dimensionless total pressure		
Re	Reynolds number		
S_φ	source term of the transport equation for φ	**Subscripts**	
T	temperature	b	bulk value
u, v, w	velocities in $z, r,$ and ϕ directions	o	reference or empty tube value
U, V, W	dimensionless velocities	w	wall value

tape results in a swirling flow, i.e., an axial vortex flow, in the tube. Since the velocity is increased by this flow, particularly near the wall, the heat transfer is promoted as a result of the increased shear stress. Displaced inserts have been used also [9]. A recent example is the short inner-tube inserts studied by Fu and Tseng [10] and Fu, Tseng, and Huang [11]. By this method, fluid is displaced closer to the outer tube wall when flowing through the passage between the inner tube and the outer tube, leading to a larger axial velocity there and, thus, higher heat transfer.

In this study, similar to that of Fu and Tseng, a short empty tube is inserted into a heat exchange tube. However, the geometry of the inner tube is deformed in a way that a convoluted trailing edge is obtained, as seen in Figure 1. As will be seen later, this convoluted geometry causes formation of a radially outward flow

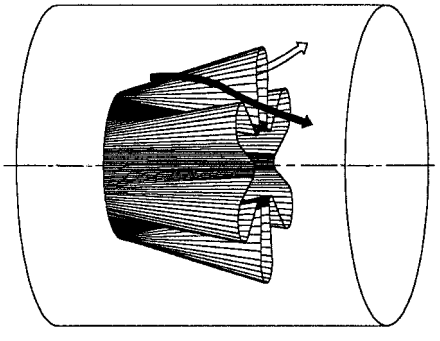

Figure 1. A drawing of the multilobe vortex generator.

inside this inner tube and a radially inward flow outside the tube. This radial and counterradial flow structure transforms to become vortex flow after flowing out of this tube. Therefore, this convoluted tube is called the multilobe vortex generator. Different from the use of twisted tape, by which a single vortex is formed, there are 2n vortices for an n-lobe vortex generator. With use of these axial vortices it has been shown that the multilobe vortex generator is effective in promoting mixing of two different velocity streams in a short distance with only a minor increase in pressure loss and has been employed as an internal exhaust gas mixer for turbofan engines [12–15].

According to the above discussion, it seems that the multilobe vortex generator provides a promising means to improve efficiency of heat exchangers. In a companion study [16] a multilobe vortex generator was inserted in a finned tube to examine its effects on the heat transfer. In the present study, smooth tube is incorporated instead, with a variety of lobe parameters being examined, including lobe penetration, lobe contour geometry, lobe length, and lobe number.

MATHEMATICAL METHOD

The flow is assumed to be steady, incompressible, and laminar. To fit the irregular geometry of the multilobe vortex generator, curvilinear coordinates are employed. Introduce dimensionless variables

$$
\begin{aligned}
Z &= \frac{z}{d} \qquad R = \frac{r}{d} \\
U &= \frac{u}{u_m} \quad V = \frac{v}{u_m} \quad W = \frac{w}{u_m} \\
P &= \frac{p}{\rho u_m^2} \qquad \theta = \frac{T - T_o}{T_w - T_o} \\
R_e &= \frac{u_m d}{\nu} \qquad P_r = \frac{\nu}{\alpha}
\end{aligned}
\tag{1}
$$

For an entity φ (standing for U, V, W, θ) the transport equation, after transformation from cylindrical coordinates $Z^i\ (= Z, R, \phi)$ to curvilinear coordinates ξ^j, can be written as

$$
\frac{1}{JR}\frac{\partial}{\partial \xi^j}(W^j \varphi) = \frac{1}{JR}\frac{\partial}{\partial \xi^j}\left[\frac{\Gamma_\varphi}{R}\left(J\alpha_k^j \alpha_k^n \frac{\partial \varphi}{\partial \xi^n}\right)\right] + S_\varphi \tag{2}
$$

where W^j is related to the cylindrical velocities U^k as

$$
W^j = J\alpha_k^j U^k \tag{3}
$$

and the tensor α_k^j is defined by

$$\alpha_k^j = \frac{R_k}{J}\left(\text{cof}\frac{\partial Z^j}{\partial \xi^k}\right) \tag{4}$$

The symbol $\text{cof}(\partial Z^j/\partial \xi^k)$ stands for the cofactor of $(\partial Z^j/\partial \xi^k)$ and

$$R_k = \begin{cases} R & Z^j = Z, R \\ 1 & Z^j = \phi \end{cases} \tag{5}$$

It is noted that the repeated indices k on the right-hand side of Eq. (4) are not summed. Detailed expressions for the equations can be seen in Ref. [17].

A drawing of the flow system is shown in Figure 2. The thickness of the vortex generator is neglected. Since the lobes of the vortex generator are arranged in a periodic manner, the computational domain encompasses a slice of half a lobe only. Symmetry boundaries are then imposed on the two side planes. The following boundary conditions are implemented in calculations.

Inlet: $U = 2(1 - 4R^2), V = W = 0,$

A fully developed profile for θ is assumed [18].

Outlet: $\partial U/\partial Z = \partial V/\partial Z = \partial W/\partial Z = \partial\theta/\partial Z = 0.$
Solid walls: $U = V = W = 0, \theta = 1.$
Symmetry boundaries: $\partial U/\partial\phi = \partial V/\partial\phi = W = \partial\theta/\partial\phi = 0.$
Axis of symmetry: $\partial U/\partial R = V = W = \partial\theta/\partial R = 0.$

The above boundary conditions at the axis of symmetry may not be appropriate for the case with an odd number of lobes because the flow is then not symmetric to the pole. However, its effects on the results are small because the flow field in the pole

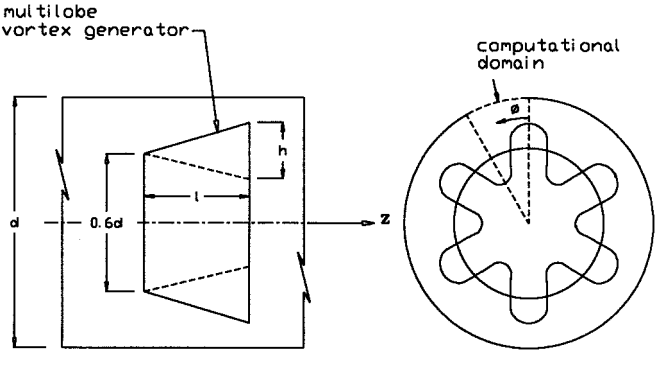

Figure 2. Configuration of the flow system.

region is quite uniform in the present study. Besides, it is difficult to assign more suitable boundary conditions there.

Discretization is performed using the finite volume method by integrating the equations over a computational control volume. A second-order linear upwind difference scheme [19] is adopted to suppress numerical diffusion. Because of the irregular lobe geometry, curvilinear nonorthogonal grids together with nonstaggered grid arrangement are employed. To avoid decoupling between pressure and velocity, which is usually encountered by using nonstaggered grids, the momentum interpolation method [20] is employed to calculate the velocity across the surfaces of the computational cell. By forcing the face velocity to satisfy the continuity equation a pressure-correction equation is obtained. A common practice is to ignore the corner point's contribution to the pressure-correction equation during the iteration [21] such that this equation can be greatly simplified. However, serious grid nonorthogonality causes difficulty in the convergence of the solution iteration. Therefore, a full pressure-correction equation, a 19-point equation, is solved in calculations.

Because of the complex lobe geometry, curvilinear three-dimensional grids are needed. The grid is constructed by first generating 2-D grids at prescribed axial locations and then stacking all these grids to form a 3-D grid. The 2-D grids are generated by solving a pair of transformed Poisson equations [22]

$$\alpha x_{\xi\xi} - 2\beta x_{\xi\eta} + \gamma x_{\eta\eta} = -J^2\left(P(\xi,\eta)x_\xi + Q(\xi,\eta)x_\eta\right) \tag{6}$$

$$\alpha y_{\xi\xi} - 2\beta y_{\xi\eta} + \gamma y_{\eta\eta} = -J^2\left(P(\xi,\eta)y_\xi + Q(\xi,\eta)y_\eta\right) \tag{7}$$

The two functions $P(\xi,\eta)$ and $Q(\xi,\eta)$ are used to control the distribution of grid points and those functions proposed by Steger and Sorenson [23] are adopted. After completing the 2-D grids, the corresponding grid points on all transverse planes are linked to form a 3-D grid. The grid lines along the axial direction might not be smooth. A smooth procedure is then undertaken. A typical grid generated by the above method is shown in Figure 3.

RESULTS AND DISCUSSION

To validate the analytical model described above, a series of tests were conducted. First, the flow in an empty, circular tube was considered. The inlet velocity was assumed to be fully developed and the inlet temperature to be uniform. Heat was added into the flow from the tube wall that was assumed fixed at a constant temperature. The resulting Nu along the wall was consistent with analytical results that could be found in textbooks. In the second test, three different inserts studied by Fu and Tseng [10] were placed in a tube to promote heat transfer. The inserts included a short annular tube, a short sudden-expansion tube, and a short sudden-contraction tube. Comparisons of the resulting Nu along the wall for the cases of circular tube insert (type III) and sudden-expansion tube insert (type IV) are presented in Figure 4. It is seen that good agreement between the two predictions is obtained, justifying the mathematical method described above.

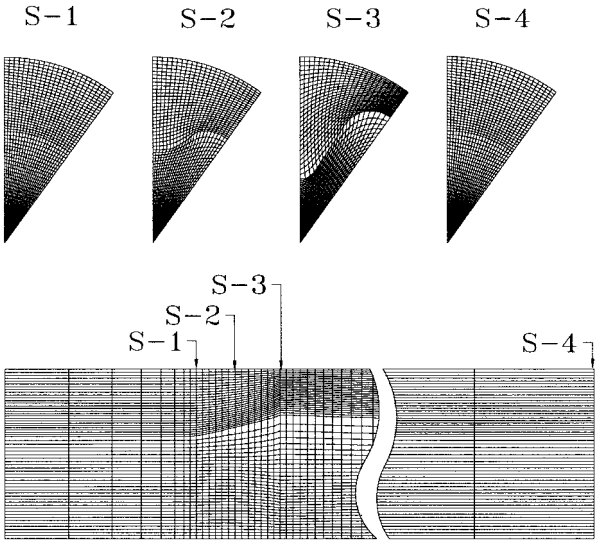

Figure 3. A computational grid.

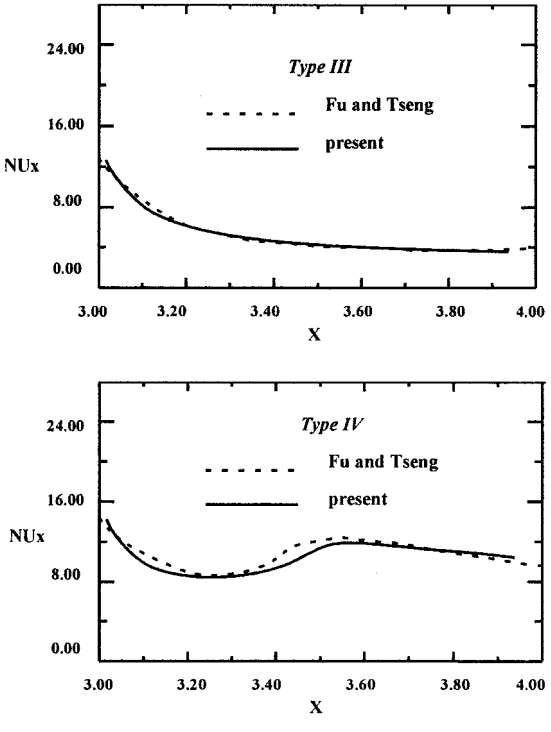

Figure 4. Comparison with the predictions of Fu and Tseng [10].

The configuration of the flow system tested was shown in Figure 2. The total length of the tube used in the computations is $7d$, and the leading edge of the vortex generator is located at $0.5d$. The inlet diameter of the vortex generator is $0.6d$. The Reynolds number (Re) of the flow is 2000, unless otherwise stated, and the Prandtl number (Pr) is fixed at 5. The geometric parameters considered include number of lobes, lobe penetration, lobe length, and lobe contour geometry, which are listed in Table 1. As mentioned before, owing to the periodic lobe geometry a slice of half a lobe is considered in the calculations.

To illustrate the flow structure a vortex generator composed of six lobes was used. The length of the vortex generator is $1d$ and the lobe penetration is $0.212d$. The lobe contour geometry is of linear shape. This vortex generator is called type A and serves as a baseline case. Grid refinement tests were performed on this type using four levels of grid. The number of grid nodes ranges from 22,500 to 120,000. The resulting variations of Nu and total pressure, which are the most important parameters used to evaluate the performance of heat exchangers, are shown in Figure 5. It is apparent that the two finest grids give close results. In the following, the predictions obtained using the finest grid $80(Z) \times 60(R) \times 25(\phi)$ are presented.

Flow Structure

The flow field is represented by the plot of velocity vectors, as shown in Figure 6. The axial plane $\phi = 0°$ is the symmetry boundary on the peak side of the lobe while the plane $\phi = 30°$ is the boundary on the trough side. The lobe is placed in the region between the stations $S_1 = 0.5$ and $S_2 = 1.5$. In addition to the axial planes, diametral planes at a number of selected locations also are shown. It is seen that when the fluid flows through the lobe it follows the lobe surface without causing separation. Secondary velocities are induced because of the convoluted shape of the lobe. A radially downward velocity toward the trough is formed outside the lobe and a radially upward velocity toward the peak is formed inside the lobe. After the flow emerges from the lobe, the radial and counterradial flow

Table 1. Tested lobe configurations

Configuration	Lobe Number(n)	Lobe Penetration(H)	Lobe Length(L)	Lobe Geometry
A-type	6	0.212	1	linear
B1-type	6	0.187	1	linear
B2-type	6	0.260	1	linear
C1-type	6	0.212	1	concave
C2-type	6	0.212	1	convex
D1-type	6	0.212	1/3	linear
D2-type	6	0.212	1/5	linear
E1-type	4	0.212	1	linear
E2-type	5	0.212	1	linear
E3-type	9	0.212	1	linear
F-type	5	0.260	1/5	concave

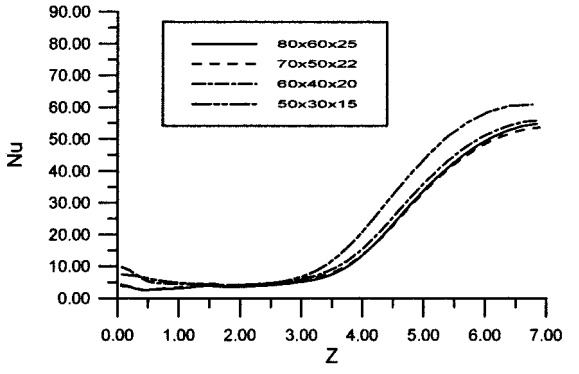

(*a*)

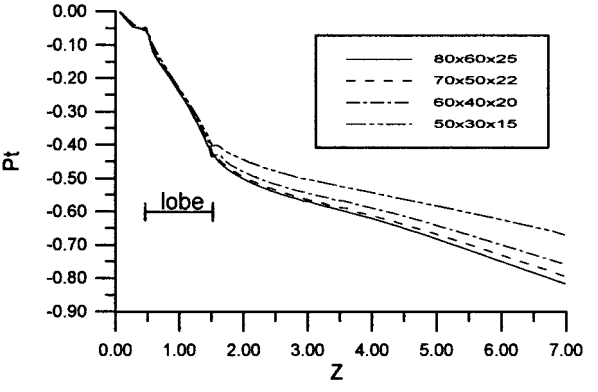

(*b*)

Figure 5. Axial variation of (*a*) Nusselt number and (*b*) total pressure for grid refinement test.

structure is transformed to become an organized axial vortex, which rotates in a counterclockwise direction, i.e., in the direction from the peak to the trough in the region near the wall. Because of viscous dissipation, the strength of the vortex flow gradually attenuates, as can be seen from the magnitude scale shown in the figure. Since the inlet flow is assumed fully developed, the axial velocity is initially small near the wall and large in the core. It can be identified that the axial velocity profiles in the $\phi = 0°$ plane gradually become flat downstream of the lobe. This phenomenon is attributed to the transport of the high-speed core flow to the wall by the circumferential velocity of the axial vortex. The distribution of temperature in diametral planes is shown in Figure 7. It is noted that in the core region, i.e., in the region near the centerline, the flow velocity is higher and the temperature is lower. As discussed above, this high-speed, low-temperature core flow at the peak side of the lobe ($\phi = 0°$) is transported by the vortex directly toward the wall, resulting in significant heat transfer there. The heat is then carried away from the wall at the trough side ($\phi = 30°$) by this vortex such that this high-temperature wall

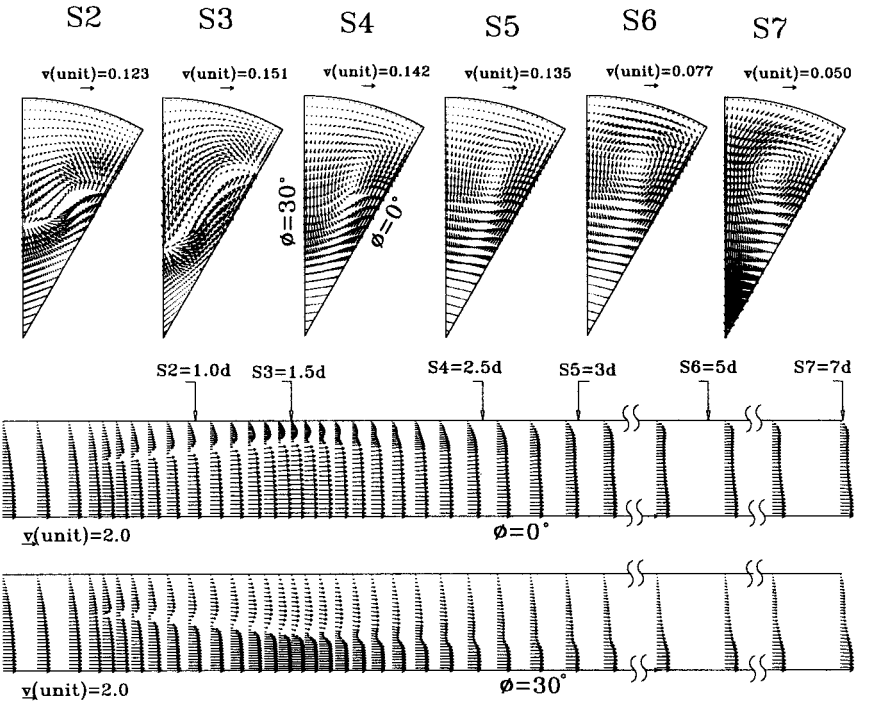

Figure 6. Velocity vectors in diametral and axial planes for type A.

flow is mixed with the low-temperature core flow. This phenomenon can be identified by viewing the curved shape of the isotherms. In this way, very effective heat transfer and flow mixing are yielded. It is pointed out here that the mechanism to cause heat transfer improvement is quite different between the multivortex flow and the single vortex flow, i.e., the swirling flow induced by twisted tapes or guided vanes. For the latter the enlarged velocity caused by the swirl enhances heat

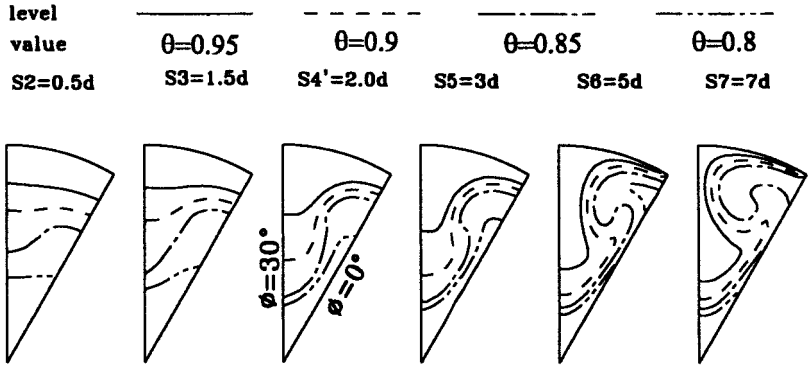

Figure 7. Isotherms in diametral planes for type A.

transfer at the wall. However, it depends totally on diffusion to transfer heat away from the wall region, which is a slow process. In the multivortex flow this process is of convection type and of course is more efficient.

Parametric Tests

Before testing the geometric parameters, a number of parameters used to characterize the flow field are defined first. It has been seen that the axial vortex is the most significant character in the flow field and plays the most important role in enhancing heat transfer and flow mixing. To quantify the strength of the vortex, the following circulation is introduced:

$$\Gamma = \oint_C \vec{V} \cdot d\vec{s} \tag{8}$$

where the circuit C denotes the outer path of the considered domain in a diametral plane, i.e., the path making up the two symmetry lines and the tube wall. Since velocity vanishes on the tube wall, the circulation is equal to the line integral of the radial velocity along the two symmetry boundaries. It is noted that by the Stokes theorem the circulation is equivalent to the integration of the axial component of vorticity over the cross-sectional area A surrounded by the circuit C:

$$\Gamma = \int_A \omega_z \, dA. \tag{9}$$

The heat transfer at the tube wall is characterized by Nu being defined as

$$\mathrm{Nu} = \frac{\dfrac{1}{\phi_{\max}} \displaystyle\int_0^{\phi_{\max}} \left.\frac{\partial \theta}{\partial R}\right|_{\text{wall}} d\phi}{(1 - \theta_b)} \tag{10}$$

where θ_b is the bulk temperature

$$\theta_b = \frac{\displaystyle\int_A U\theta \, dA}{\displaystyle\int_A U \, dA} \tag{11}$$

The wall shear stress is represented by the skin friction coefficient

$$C_f = \frac{\tau_w}{\frac{1}{2}\rho U_m^2} \tag{12}$$

where the stresses on both the tube wall and the lobe surface are included.

The total pressure, defined below, is based on a flux-averaged form:

$$P_t = \frac{\int_A U\left(P + \frac{1}{2}\rho U^2\right) dA}{\int_A U\, dA} \tag{13}$$

where only the axial velocity component is considered in the dynamic pressure.

Effects of lobe penetration. The penetration h is defined as the height between the peak and the trough at the trailing edge (see Figure 2). The penetrations considered are $h/d = 0.212, 0.187$, and 0.26 for types A, B1, and B2, respectively (see Table 1). The variation of circulation along the axis is shown in Figure 8*a*. The radial and counterradial velocities induced by the convoluted lobe result in generation of circulation. The development of the radial velocities and, thus, the circulation reaches its highest point at the trailing edge of the lobe. The large penetration of B2 type leads to the highest level of circulation, whereas the circulation of B1 type is the lowest. The cause of high circulation by increasing the penetration is ascribed to the increase of the slope of the lobe contour, which, in turn, induces larger radial velocities because, provided that no serious boundary layer separation takes place, the flow will follow the lobe surface contour.

The variation of Nu along the tube wall is given in Figure 8*b*. It is important to notice that although large radial velocities and circulation form at the exit of the vortex generator, it takes time to complete an organized swirling flow such that the high-speed, low-temperature core flow can sweep across the tube wall. Therefore, the augmentation of Nu starts not at the exit of the lobe, but at a certain distance downstream. However, the larger the circulation, the quicker the formation of the vortex. Therefore, the rise of Nu for the B2-type vortex generator occurs earlier than other types. Besides, the large circulation of B2 type yields more effective heat transfer.

Figure 8*c* presents the variation of skin friction coefficient. The flow through the vortex generator results in large friction in the lobe region. Also because of the transport of the high-speed core flow to the wall by the axial vortex, the friction is enhanced at some distance downstream of the lobe. As expected, this distance is shorter and the extent of augmentation is larger for B2 type.

The effect of friction is to cause total pressure loss. The large friction in the lobe region results in rapid decrease in pressure, followed by a much lower loss downstream of the lobe in Figure 8*d*. The higher pressure loss of the B2-type lobe simply reflects that it is a more effective vortex generator and heat exchanger. It is especially apparent from the B2 curve that the pressure loss rate becomes higher when the friction augmentation occurs.

Effects of lobe contour geometry. The contour geometry of the A-type lobe is of linear shape. Two other configurations are considered. The C1 type varies in a concave manner and the C2 type in a convex way (see Table 1 and Figure 9). The variations of circulation and Nu are given in Figures 10*a* and 10*b*, respectively. The circulation of C1 type continues to increase until the end of the lobe and becomes the largest among the three. For the C2 type the circulation

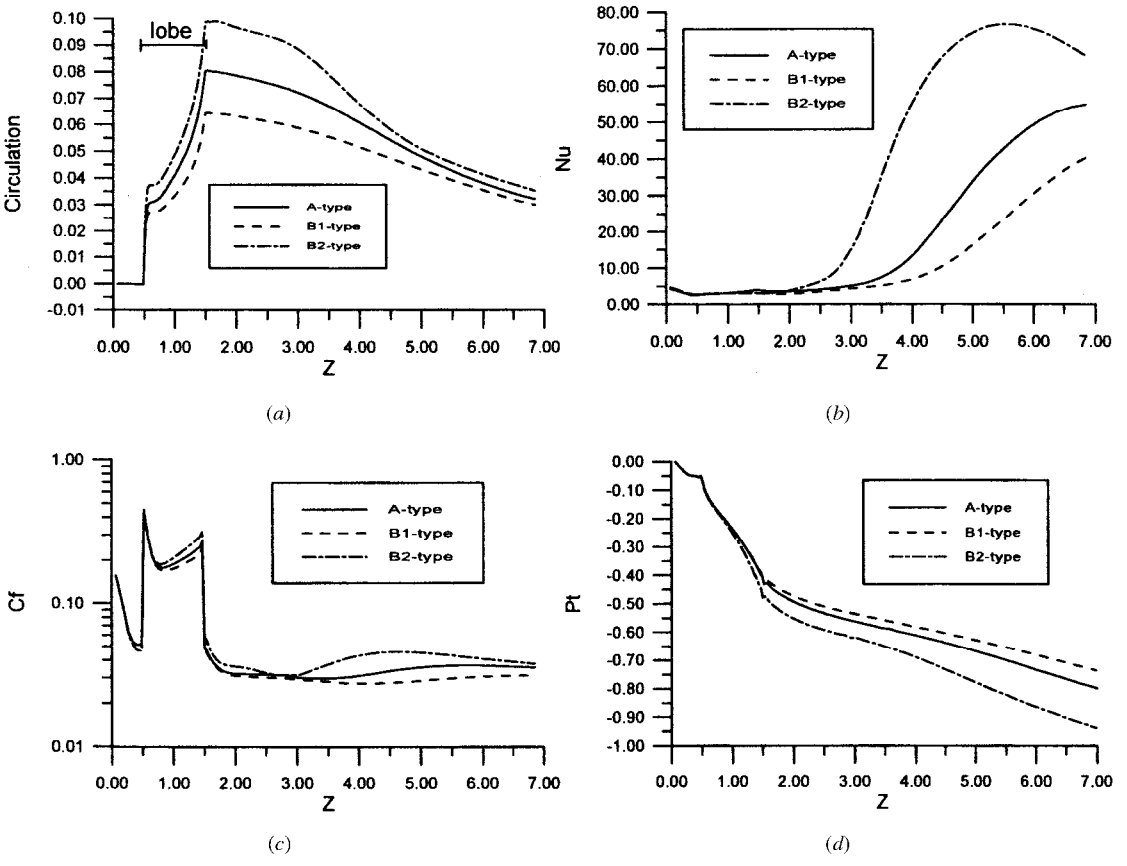

Figure 8. Axial variation of (*a*) circulation, (*b*) Nusselt number, (*c*) skin friction coefficient, and (*d*) total pressure for the test of lobe penetration.

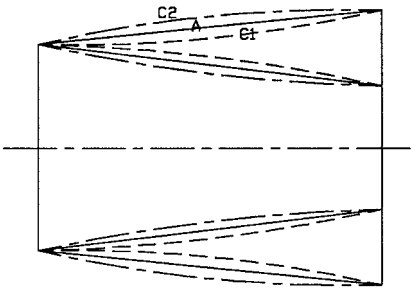

Figure 9. Lobe contour geometry for types A, C1, and C2.

builds up quickly first and then declines in the rest region of the lobe, leading to the lowest level of circulation. These results will not be surprising by examining the slopes of the two lobes and understanding that the flow more or less follows the shape of the lobe. The slope of the concave shape of C1 type increases continuously along the axis, whereas that of C2 type decreases. Because the vortex

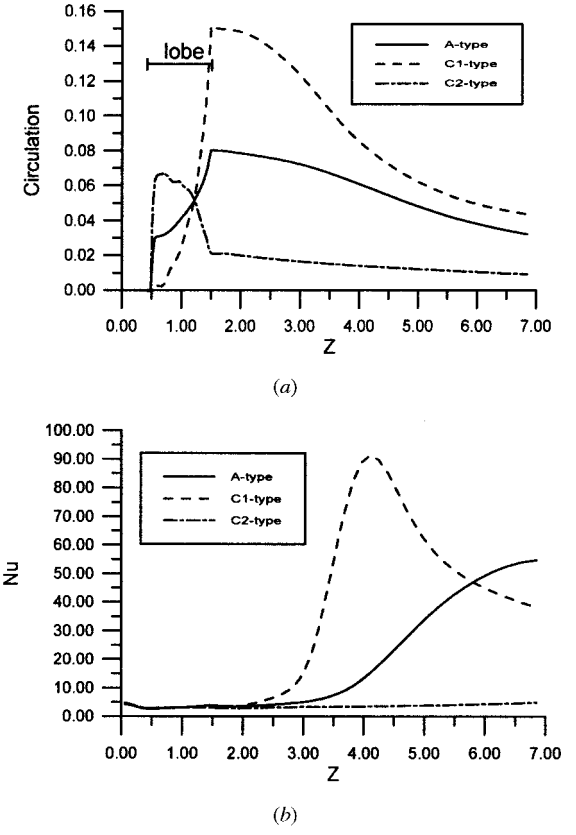

Figure 10. Axial variation of (*a*) circulation and (*b*) Nusselt number for the test of lobe contour geometry.

strength is so weak, there is no heat transfer enhancement taking place in the C2 type, as seen in Figure 10*b*. The strong vortex flow induced by the C1 type helps to improve both the heat transfer and the friction (not shown) significantly and, therefore, causes larger pressure loss (not shown).

Effects of lobe length. The length of the A-type lobe is 1*d*. The length is reduced to $d/3$ and $d/5$ for types D1 and D2 (see Table 1). When the length is reduced, the slope of the lobe is increased. As a consequence, the level of circulation at the lobe exit is greatly promoted as seen in Figure 11*a*. However, the strength of the vortex also decays fast downstream of the lobe. It turns out that both D1 and D2 types have a large Nu peak but with a quick attenuation following (see Figure 11*b*).

Effects of lobe number. The baseline case (type A) has six lobes. The numbers of lobes for types E1, E2, and E3 are four, five, and nine, respectively (see Table 1). The variations of circulation and Nu are presented in Figure 12. With

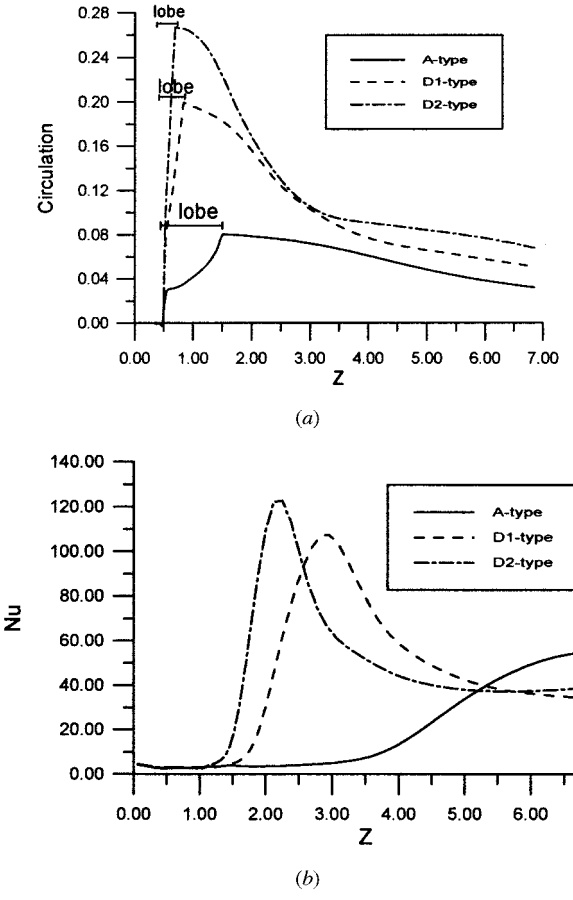

Figure 11. Axial variation of (*a*) circulation and (*b*) Nusselt number for the test of lobe length.

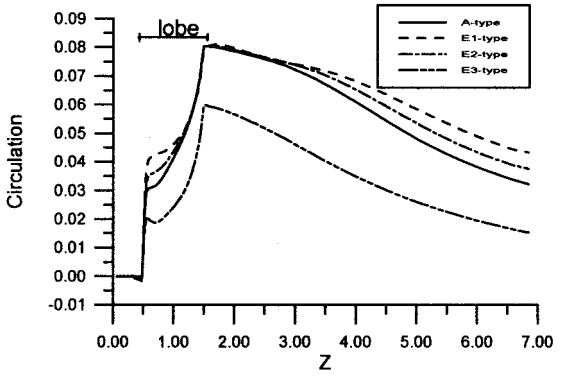

(*a*)

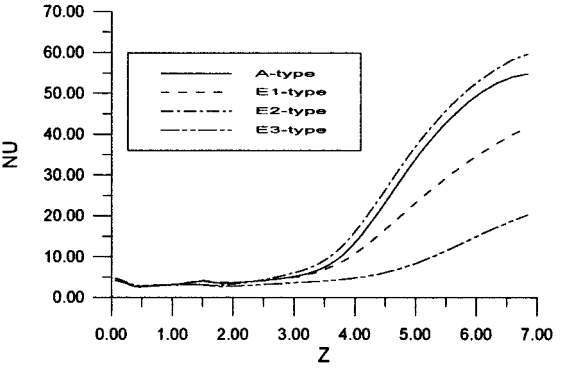

(*b*)

Figure 12. Axial variation of (*a*) circulation and (*b*) Nusselt number for the test of lobe number.

nine lobes in the E3 type the flow passage in the lobe is greatly narrowed, which restricts the development of the secondary velocities and the circulation. Therefore, the heat transfer for the E3 type is poor. It is interesting to notice that although the E1 type has the largest circulation, the enhancement of Nu is not as effective as that for A and E2 types. Among the five choices, the E2 type is the most preferable.

An optimum configuration. According to the above tests, the best configured design is proposed (see Figure 13). The vortex generator, termed type F (see Table 1), features a concave geometry with five lobes. The penetration is $0.26d$ and the total length $0.2d$. It is apparent from Figure 14 that the circulation is greatly increased and, consequently, the heat transfer is much improved. The temperature distribution at a number of downstream locations is shown in Figure 15, while the plot for the A type can be seen in Figure 7. Obviously, because of the convection transport of the strong vortex, the F type is very effective in mixing the hot wall flow and cold core flow, leading to a much more uniform distribution of temperature at the exit of the tube than that of type A.

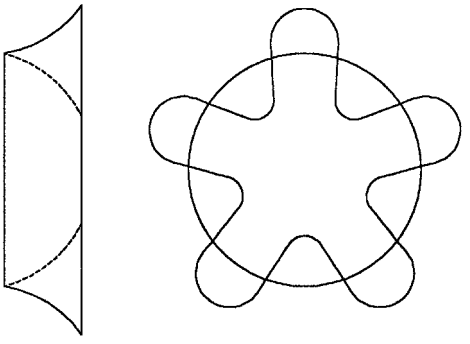

Figure 13. Lobe contour geometry for type F.

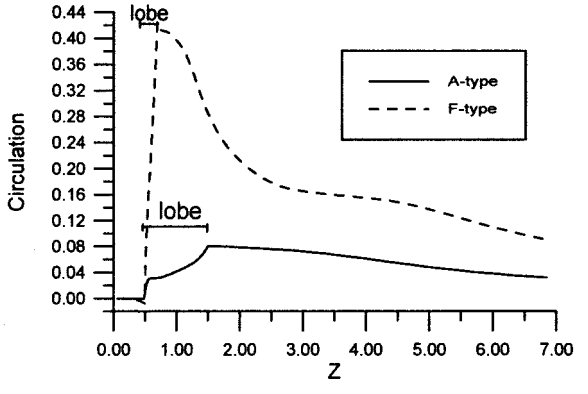

(*a*)

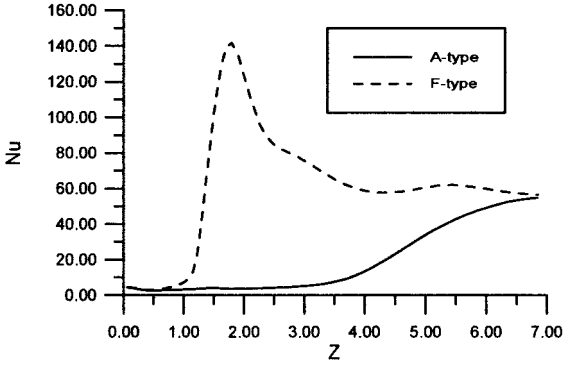

(*b*)

Figure 14. Axial variation of (*a*) circulation and (*b*) Nusselt number for comparison of types A and F.

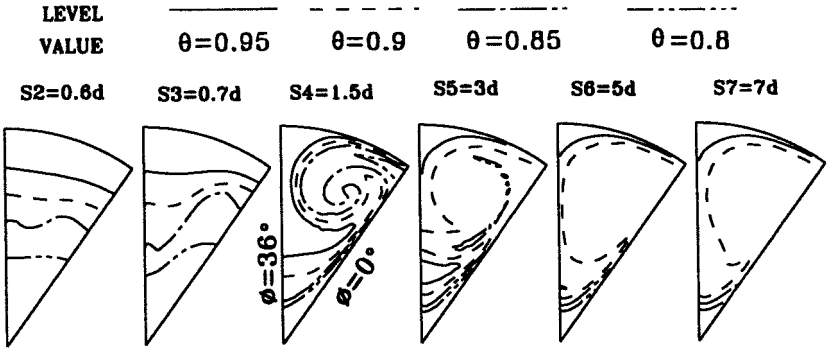

Figure 15. Isotherms in diametral planes for type F.

Performance Evaluation

The performances of all types of lobes considered are summarized in Table 2. In this table $\overline{\mathrm{Nu}}$ stands for the Nu averaged over the entire tube wall, and f is the friction factor, defined as

$$f = \frac{\Delta P}{\frac{1}{2}\rho U_m^2}\frac{d}{l_t} \tag{14}$$

where ΔP is the pressure drop between the tube inlet and tube outlet. E and F are the heat transfer enhancement factor and the friction penalty factor, respectively, defined by

$$E = \frac{\overline{\mathrm{Nu}}}{\mathrm{Nu}_0} \tag{15}$$

$$F = \frac{f}{f_0} \tag{16}$$

where $\mathrm{Nu}_0 = 3.66$ and $f_0 = 64/\mathrm{Re}$ denote the Nu and friction factor, respectively, of a fully developed laminar flow in a smooth empty tube. Finally, the parameter in the last column of Table 2 represents the efficiency index:

$$\eta = \frac{E}{F} \tag{17}$$

which is used to evaluate the quality of the enhancement. It can be seen from the table that apart from C2 and E3 types, all efficiency indices are greater than 1. Among the parameters tested, the reduction of lobe length and the use of the concave contour is the most effective because the slope of the lobe can be greatly increased. It is noticed that although D2 type has shorter length, its efficiency index is lower than that for D1 type because it has larger pressure loss and, thus, a

Table 2. Performance for tested cases

Configuration	$\overline{Nu}$	$f(\times 10^{-2})$	E	F	η
A-type	20.	11.7	5.5	3.7	1.5
B1-type	12.5	10.5	3.4	3.3	1.0
B2-type	38.3	13.4	10.5	4.2	2.5
C1-type	34.6	17.6	9.5	5.5	1.7
C2-type	3.6	11.	1.	3.4	0.3
D1-type	42.6	12.9	11.6	4.	2.9
D2-type	43.5	13.9	11.9	4.3	2.7
E1-type	16.5	10.5	4.5	3.3	1.4
E2-type	21.8	11.	6.	3.5	1.7
E3-type	7.2	11.6	2.	3.6	0.5
F-type	59.6	17.4	16.3	5.4	3.

greater friction factor. Comparing type F with type A, the efficiency index is doubled.

In the above tests Re is fixed at 2000. The performance at lower values of Re for type A is shown in Table 3. When Re decreases, both the heat transfer enhancement factor and the friction penalty factor decrease. However, the efficiency index remains nearly constant.

CONCLUSIONS

A 3-D numerical procedure has been successfully developed to examine the flow and heat transfer resulting from multilobe vortex generators inserted in a circular tube. Based on the calculated results, the following conclusions are drawn.

1. Because of the secondary velocities induced by the lobes, axial vortices form downstream of the lobes. When the vortices are well developed at a distance downstream of the lobes, the heat transfer as well as the wall friction are greatly enhanced. The cause of enhancement is attributed mainly to the transport of the high-speed, low-temperature core flow by the vortex flow to sweep across the wall. Also because of the convection transport of the vortex flow, the high-temperature wall flow is quickly mixed with the low-temperature core flow.
2. The extent of heat transfer/friction augmentation is related directly to the strength, or the circulation, of the induced axial vortices. High circulation

Table 3. Effects of Reynolds number on performance

Re	$\overline{Nu}$	$f(\times 10^{-2})$	E	F	η
2000	20.	11.7	5.5	3.7	1.5
1500	18.4	14.5	5.0	3.4	1.5
1000	13.2	14.9	3.6	2.3	1.6

can be obtained by increasing the lobe penetration, reducing the lobe length, and making a concave contour geometry because the slope of the lobe is increased with these modifications. Although more axial vortices can be induced when the number of lobes is increased, the resulting narrow lobe passage may restrict the development of the vortex.

It should be addressed here that the multilobe vortex generator is very effective only in a short distance because the axial vortex will die away far downstream. For a heavy-duty heat exchanger the multilobe vortex generator can cooperate with, say, a finned tube, and a number of vortex generators can be inserted into the tube in an array to improve greatly heat transfer.

REFERENCES

1. R. L. Webb, E. R. G. Eckert, and R. J. Goldstein, Heat Transfer and Friction in Tubes with Repeated-Rib Roughness, *Int. J. Heat Mass Transfer*, vol. 14, pp. 601–617, 1971.
2. D. L. Gee and R. L. Webb, Forced Convection Heat Transfer in Helically Rib-Roughened Tubes, *Int. J. Heat Mass Transfer*, vol. 23, pp. 1127–1136, 1980.
3. R. Sethumadhavan and M. Raja Rao, Turbulent Flow Heat Transfer and Fluid Friction in Helical-Wire-Inserted Tubes, *Int. J. Heat Mass Transfer*, vol. 26, pp. 1833–1845, 1983.
4. R. L. Webb and M. J. Scott, A Parametric Analysis of the Performance of Internally Finned Tubes for Heat Exchanger Application, *ASME J. Heat Transfer*, vol. 102, pp. 38–43, 1980.
5. G. J. Rowley and S. V. Patankar, Analysis of Laminar Flow and Heat Transfer in Tubes with Internal Circumferential Fins, *Int. J. Heat Mass Transfer*, vol. 27, pp. 553–560, 1984.
6. R. F. Lopina and A. E. Bergles, Heat Transfer and Pressure Drop in Tape-Generated Swirl Flow of Single-Phase Water, *ASME J. Heat Transfer*, vol. 91, pp. 434–442, 1969.
7. A. W. Date, Prediction of Fully-Developed Flow in a Tube Containing a Twisted-Tape, *Int. J. Heat Mass Transfer*, vol. 17, pp. 845–859, 1974.
8. N. S. Gupte and A. W. Date, Friction and Heat Characteristics of Helical Turbulent Air Flow in Annuli, *ASME J. Heat Transfer*, vol. 111, pp. 337–344, 1989.
9. R. L. Webb, Principles of Enhanced Heat Transfer, John Wiley & Sons, New York, 1994.
10. W.-S. Fu and C.-C. Tseng, Enhancement of Heat Transfer for a Tube with an Inner Tube Insertion, *Int. J. Heat Mass Transfer*, vol. 37, pp. 499–509, 1994.
11. W.-S. Fu, C.-C. Tseng, and C.-S. Huang, Experimental Study of the Heat Transfer Enhancement of an Outer Tube with an Inner-Tube Insertion, *Int. J. Heat Mass Transfer*, vol. 38, pp. 3443–3454, 1995.
12. P. K. Shumpert, *An Experimental Model Investigation of Turbofan Engine Internal Exhaust Gas Mixer Configuration*, AIAA Paper 80-0228, 1980.
13. R. W. Paterson, Turbofan Mixer Nozzle Flow Field—A Benchmark Experimental Study, *ASME J. Engineering Gas Turbines and Power*, vol. 106, pp. 692–698, 1984.
14. D. C. McCormick and J. C. Bennett, Jr., Vortical and Turbulent Structure of a Lobed Mixer Free Shear Layer, *AIAA J.*, vol. 32, pp. 1852–1859, 1994.
15. Y.-Y. Tsui and P.-W. Wu, Investigation of the Mixing Flow Structure in Multilobe Mixers, *AIAA J.*, vol. 34, pp. 1386–1391, 1996.
16. Y.-Y. Tsui and S.-W. Leu, Heat Transfer Enhancement by a Multilobe Vortex Generator in Internally Finned Tubes, *Numer. Heat Transfer, Part A*, vol. 35, pp. 553–566, 1999.

17. Y.-Y. Tsui, P.-W. Wu, and C.-W. Liao, Flow Modeling in Turbofan Mixing Duct, *Numer. Heat Transfer*, *Part A*, vol. 26, 219–236, 1994.
18. A. Bejan, *Convection Heat Transfer*, John Wiley & Sons, New York, 1984.
19. Y.-Y. Tsui, A Study of Upstream-Weighted High-Order Differencing for Approximation to Flow Convection, *Int. J. Numer. Methods Fluids*, vol. 13, pp. 167–199, 1991.
20. C. M. Rhie and W. L. Chow, A Numerical Study of the Turbulent Flow Past an Isolated Airfoil with Trailing Edge Separation, *AIAA J.*, vol. 21, pp. 1525–1532, 1983.
21. M. Peric, Analysis of Pressure-Velocity Coupling on Nonorthogonal Grids, *Numer. Heat Transfer*, *Part B*, vol. 17, pp. 63–82, 1990.
22. J. F. Thompson, *Numerical Grid Generation-Foundations and Applications*, North-Holland, New York, 1985.
23. J. L. Steger and R. L. Sorenson, Automatic Mesh-Point Clustering Near a Boundary in Grid Generation with Elliptic Partial Differential Equations, *J. Comput. Physics*, vol. 33, pp. 405–410, 1979.